EES Solar

Accepted Manuscript

This article can be cited before page numbers have been issued, to do this please use: A. Wsiak-Maciejak, M. cigaj, K. Bakker, D. Roosen-Melsen, . Przypis, K. Dyk, P. Janicka, K. Rycek, D. Takhellambam, A. Di Carlo and K. Wojciechowski, *EES Sol.*, 2026, DOI: 10.1039/D6EL00050A.

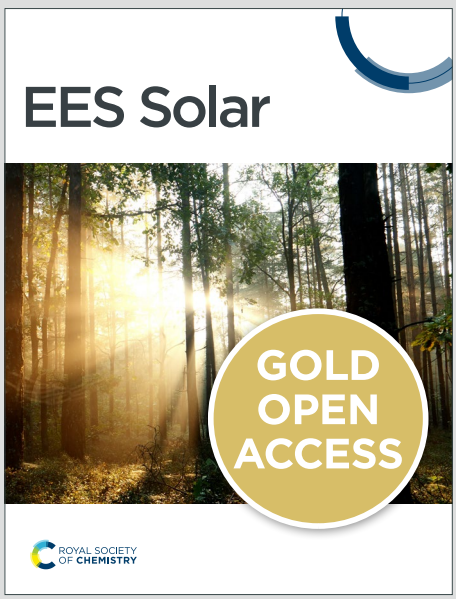

View Article Online
DOI: 10.1039/D6EL00050A

Broader context

The global transition to renewable energy demands photovoltaic technologies that go beyond rooftop and ground-mounted installations. Lightweight, flexible solar modules can be integrated onto building facades, vehicles, portable devices, and other curved or weight-sensitive surfaces - applications where conventional rigid silicon panels are impractical. Perovskite semiconductors, which can be deposited from solution at low temperatures, are uniquely suited for manufacturing such flexible devices using high-throughput roll-to-roll processes on inexpensive plastic foils. However, moving from efficient small-area laboratory cells to large-area modules that remain stable under real-world heat and humidity has proven difficult, and reports demonstrating the full fabrication-to-encapsulation chain on flexible substrates remain scarce. This work addresses that gap by presenting a complete, industrially compatible process for blade-coated perovskite solar modules on plastic foils, achieving module efficiencies above 15% for two different absorber bandgaps and demonstrating that encapsulated devices retain 80% of their initial performance after over 1000 hours of harsh damp-heat testing. By bridging laboratory-scale results with production-relevant fabrication and packaging methods, this study provides a practical blueprint for manufacturing durable, lightweight perovskite photovoltaics at scale.

View Article Online
DOI: 10.1039/D6EL00050A

Efficient inverted FA–Cs perovskite solar modules fabricated by blade-coating on PET foils with robust encapsulation

Received 00th January 20xx,
Accepted 00th January 20xx

DOI: 10.1039/x0xx00000x

Anna Wąsiak-Maciejak[a,b], Mateusz Ścigaj[a], Klaas Bakker[c], Dorrit Roosen-Melsen[c], Łukasz Przypis[a,d,e], Konrad Dyk[a], Patrycja Janicka[f], Kinga Rycek[f], Daimiota Takhellambam[b], Aldo Di Carlo[b,g], and Konrad Wojciechowski*[a,d,e]

The commercial deployment of perovskite photovoltaics (PV) hinges on bridging the gap between high-efficiency lab-scale devices and scalable, reliable modules. While flexible polymeric substrates offer a pathway to high-throughput roll-to-roll (R2R) manufacturing, achieving long-term operational stability on these platforms remains a critical challenge. Here, we report a robust strategy for the scalable manufacturing of efficient inverted formamidinium-cesium (FA-Cs) flexible perovskite solar modules (FPSMs), complemented by an industrially compatible encapsulation sequence. By employing a modified gas-assisted blade-coating process, combined with a gradual annealing protocol utilizing the thermal mass of a PDMS-covered copper plate (≤100°C), we demonstrate a unified processing framework applicable to FA–Cs perovskite compositions of different bandgaps. In the device architecture, we employed a synergistic interface engineering approach utilizing the self-assembling molecule 4-((5H-diindolo[3,2-a:3',2'-c]carbazole-5,10,15-triyl)tris(butane-4,1-diyl))tris(phosphonic acid) (TRIPOD-C4) as an effective hole-transporting layer, combined with propane-1,3-diammonium iodide ($PDAI_2$) for perovskite surface passivation. As a result, blade-coated FA–Cs PSCs with bandgaps of 1.61 eV and 1.76 eV achieved power conversion efficiencies (PCEs) of 20.4% and 17.4%, respectively. When scaled to modules, we recorded champion efficiencies of 17.0% and 15.1% for the medium- and wide-bandgap absorbers, respectively. Furthermore, we demonstrate a production-compatible vacuum lamination protocol utilizing ultra-high barrier foils. The encapsulated FPSMs exhibit promising durability, retaining 80% of their initial efficiency after 1026 hours of damp-heat aging (ISOS-D3, 85 °C/85% RH).

Introduction

Metal halide perovskite solar cells (PSCs) have rapidly ascended as a frontrunner in the next generation of photovoltaics, demonstrating the fastest increase in certified power conversion efficiency (PCE) among all PV technologies.[1–3] PSCs are characterized by a unique combination of exceptional optoelectronic properties of the perovskite absorbing material and commercially attractive solution processability, with low-temperature post-processing.[4–7] This enables the utilization of lightweight polymeric foils, such as polyethylene terephthalate (PET) or polyethylene naphthalate (PEN), which in turn unlocks high-throughput roll-to-roll (R2R) manufacturing.[8] The vast majority of reported data on perovskite PV devices is centered on those fabricated via spin-coating, a method not transferable to industrial production.[9,10] To enable large-scale manufacturing, it is essential to adopt scalable deposition techniques (such as slot-die coating, blade coating, spray coating, or inkjet printing) that minimize material waste and provide uniform coatings over larger areas.[10,11] These deposition techniques are well-suited for integration into a continuous R2R production process on flexible substrates.[12–14] Besides manufacturing innovations and implied cost efficiency, flexible PV devices offer a high power-to-weight ratio and large design versatility, which provide additional value propositions for numerous commercial use cases.[15–17] Mechanical conformability enables lightweight integration onto curved surfaces, textiles, and portable or airborne platforms.[18–20] While certified efficiencies for small-area cells now rival those of crystalline silicon, translating these performance metrics to large-area modules, particularly on flexible substrates, presents distinct engineering challenges.[10,21] The difficulty arises from the complex interplay of reduced control over nucleation and crystallization dynamics and a prolonged wet-film phase while processing large areas, especially when compared to spin-coating small-area samples.[22–24] This challenge is further exacerbated for perovskite compositions, such as the double-cation formamidinium-cesium (FA-Cs) systems, and those with high bromine content (typically used for wider bandgap perovskites), where the differences in solubilities and ionic radius of the precursor components result in rapid and inhomogeneous crystallization.[25–30] Furthermore, fabricating highly efficient devices on flexible substrates remains more demanding than on rigid counterparts.[8,13] This is related to the properties of the substrate itself, but also to the substrate handling. The most commonly used and most economical PET foils impose inherent thermal constraints on the device fabrication process, owing to their thermal

[a] Saule Research Institute, Duńska 11, 54-427 Wrocław, Poland.
[b] CHOSE – Centre for Hybrid and Organic Solar Energy, Department of Electronic Engineering, University of Rome "Tor Vergata", Via del Politecnico 1, 00133, Rome, Italy.
[c] TNO, Netherlands Organisation for Applied Scientific Research, Solar Technologies and Applications, High Tech Campus 21, 5656AE, The Netherlands.
[d] Department of Semiconductor Materials Engineering, Wroclaw University of Science and Technology, Wybrzeże Wyspiańskiego 27, 50-370 Wrocław, Poland.
[e] Chemini, 1 Maja 92A, Rosnówko, 62-052 Komorniki, Poland.
[f] Saule Technologies, Duńska 11, 54-427 Wrocław, Poland.
[g] Istituto di Struttura della Materia- Consiglio Nazionale delle Ricerche Roma (ISM-CNR), 00133 Rome, Italy.

View Article Online
DOI: 10.1039/D6EL00050A

deformations (thermal expansion, release of frozen-in strains, etc.).[8,31] Furthermore, the mismatch in thermal expansion coefficients between the polymeric substrate and deposited layers can generate substantial internal mechanical stresses within the device stack at elevated temperatures.[8,32] This mismatch must be carefully considered during both device fabrication and subsequent lamination. Most reported encapsulation protocols are optimized for rigid devices with glass–glass lamination stacks, and are not suitable for flexible architectures.[33–37] To maintain the key qualities of flexible devices, lamination protocols employing ultra-low-permeability barrier foils and mechanically compliant adhesives are essential.[38] Moreover, minimizing strain accumulation and reducing the temperature during the lamination process are critical. In this context, damp heat (DH; 85 °C/85% RH) testing serves as a rigorous, industry-standard accelerated-aging protocol.[39] It combines heat and moisture to activate the main extrinsic degradation pathways in perovskite PV devices. During DH stress, water vapor ingress and high temperature accelerate perovskite decomposition and lower the activation barriers for ion migration, thereby destabilizing interfaces and the bulk material.[40,41] Performance failure is often caused by the edge ingress: moisture enters through imperfect seals and spreads inward.[42–44] Flexible modules face additional challenges, as differences in thermal expansion can cause delamination and microcracks, creating new moisture entry points.[8,45] Bending and residual thermo-mechanical stresses further facilitate defect formation and interfacial separation, linking mechanical damage to faster moisture-driven chemical and ionic degradation.[35,45,46]

In recent years, PSCs with an inverted (p–i–n) architecture have attracted significant research interest, driven by major advancements in device stack engineering and corresponding improvements in performance parameters, as well as their inherent compatibility with high-efficiency tandem configurations.[47,48] Nevertheless, there remains a notable knowledge gap regarding the scalable fabrication of flexible PV modules – a variant of perovskite technology with substantial commercial potential.[49–53] Mature photovoltaic technologies typically follow an inverse scaling law, with efficiency dropping by less than 1% with an increase of device area by an order of magnitude.[54] Although substantial progress has been made in narrowing the efficiency gap for flexible PSCs, achieving devices that are both sufficiently efficient and stable at scale remains a key challenge.

Herein, we report the scalable fabrication of efficient and stable inverted FA-Cs PSCs and PSMs. This work details the entire process, including solution blade-coating on large-area polymeric foils and subsequent device lamination with barrier foils, compatible with production-scale processes. Solution deposition was conducted directly on unsupported (free-standing) foils, with a maximum post-deposition thermal annealing of 100 °C. Building on our previous work, we utilized the self-assembling molecule (SAM) 4-((5H-diindolo[3,2-a:3',2'-c]carbazole-5,10,15-triyl)tris(butane-4,1-diyl))tris(phosphonic acid) (TRIPOD-C4) as a hole-transporting layer, which significantly improved the devices' fill factor.[55] We further incorporated propane-1,3-diammonium iodide ($PDAI_2$) to passivate the top surface of the perovskite layer. This approach enabled blade-coated FA-Cs PSCs with bandgaps of 1.61 eV and 1.76 eV, exhibiting PCEs of 20.4% and 17.4%, respectively. The optimized layer stack and processing sequence were successfully transferred to large-area modules, achieving champion efficiencies of 17.0% (E_g = 1.61 eV) and 15.1% (E_g = 1.76 eV). Furthermore, the laminated modules demonstrated robust reliability against moisture and elevated temperature, retaining up to 80% of their initial performance after 1026 hours of rigorous damp heat (ISOS-D3) testing (85°C, 85% relative humidity). In this study, we combine blade-coating on free-standing PET foils, application of the same processing parameters to two perovskite compositions, vacuum lamination, and degradation analysis under damp-heat conditions within a single workflow.

Results and discussion

Solar cells blade-coating

We employed the inverted device architecture of the following structure: polyethylene terephthalate coated with indium tin oxide (PET-ITO)/nickel oxide (NiO_X)/self-assembling molecule (SAM)/perovskite/fullerene (C_{60})/bathocuproine (BCP)/silver (Ag) (Figure 1a). The NiO_X and SAM layers were sequentially blade-coated on 18.5 × 29.0 cm^2 substrates, which were subsequently sectioned into six equal pieces, each approximately 90 cm^2, for deposition of the perovskite layer using gas-assisted blade coating.

Initially, we focused on blade-coating the wide-bandgap (WBG) perovskite. The perovskite composition, precursor solvent system, and additives were kept identical to those previously reported for WBG PSCs fabricated via spin-coating with gas-quenching, ensuring direct comparability between the two deposition methods and highlighting the importance of developing scalable fabrication techniques by mimicking large-area deposition conditions during small-area device fabrication.[55] The WBG perovskite of nominal composition $Cs_{0.2}FA_{0.8}Pb(I_{0.65}Br_{0.35})_3$ displayed an optical bandgap of 1.76 eV (Figure S1, Supporting Information). To ensure uniform hotplate annealing of the perovskite, the heating surface was covered with polydimethylsiloxane (PDMS), following the approach reported by Oh Yeong Gong et al.[56] This enabled sample planarization and prevented air gaps beneath the substrate, while allowing non-destructive transfer without inducing mechanical strain. To obtain compact and uniform films with low surface roughness, we systematically optimized the blade-coating speed and coating gap to control wet-film thickness. Two modifications to the conventional blade-coating process were introduced to improve control over the formation and conversion of the intermediate phase. First, a shielding element was mounted perpendicular to the deposition surface directly behind the blade, with a narrow gap maintained between its lower edge and the substrate (Figure 1b). This element acts as a physical barrier between the liquid meniscus and the air-knife, decoupling the initial film deposition from the gas-quenching step and creating a more controlled evaporation environment around the deposition area. Second, a gradual annealing protocol was

View Article Online DOI: 10.1039/D6EL00059A

implemented in which the sample, planarized on a PDMS-covered copper plate pre-cooled to approximately 20°C, was placed directly on a hot plate set to 100°C (Figure 1c). The thermal mass of the copper plate causes the sample temperature to rise gradually from room temperature to the target annealing temperature, effectively extending the low-temperature conversion window. This approach is particularly well-suited to flexible PET substrates: conventional gradient annealing typically requires transferring the sample between two hotplates held at different temperatures, which, for flexible foils, risks mechanical damage at each transfer step. Here, the sample remains continuously adhered to the heating surface throughout the annealing process thanks to the conformal adhesion of the PDMS layer, providing planarization and eliminating repeated attachment and detachment steps, making the protocol gentler and more practical for large-area flexible devices.

The impact of the two processing modifications on film quality and device performance was assessed. Introduction of the shielding element improved lateral film uniformity, as evidenced by spectroscopic ellipsometry thickness maps recorded over the central area of the substrate, which showed a reduced spread of thickness deviation from the mean value (Figure S2, Supporting Information). Concurrently, XRD patterns of the annealed films showed reduced reflex intensities at 8.12° and 11.4° relative to the unshielded reference (Figure S3). We assign the feature at 8.12° to the solvent-coordinated intermediate phase (likely a solvated lead halide framework), consistent with reflections reported in the 8-9° 2θ range for both DMF and NMP-based perovskite precursor systems, and the feature at 11.4° to the δ-phase of the FA-Cs composition.[57–60] The persistence of the solvent-coordinated intermediate in the annealed film is consistent with the reported thermal stability of lead halide solvent adducts formed in DMF/NMP-based precursor systems, whose complete decomposition has been shown to require temperatures exceeding 100°C.[59,60] The blade modification prevents non-uniform evaporation induced by turbulent gas flow from the air-knife. The concurrent decrease in both the 8.12° and 11.4° peaks suggests that the reduced volatilization rate affects the formation of the intermediate phase, supporting a transition to the desired α-phase rather than being trapped as a residual solvate or contributing to the formation of the δ-phase. However, the precise mechanism introduced by the shielding element requires further investigation. Additionally, a gradual annealing step was introduced to ensure controlled solvent removal and uniform film formation. Both the 8.12° and 11.4° reflexes were absent in the gradually annealed films (Figure S4a, Supporting Information), indicating that the gradual temperature rise effectively extends the low-temperature crystallization window, providing a wider temporal range for the system to navigate the complex solvate-to-perovskite transition. While the suppression of the 8.12° reflex indicates a more complete conversion of the intermediate solvate, the concurrent disappearance of the 11.4° feature suggests that the gradual temperature rise reduces the δ-phase formation. We assume this behaviour aligns with a kinetic regime where a slower, more controlled solvent removal favours direct crystallization into the α-phase. This is consistent with previous reports on intermediate-phase control in DMF/NMP-based precursor systems, where stabilising the solvent-coordinated intermediate phase is essential to suppress the formation of non-perovskite phases during crystallization.[59,61] SEM imaging revealed larger perovskite domains in the gradually annealed films (Figure S4b, Supporting Information), consistent with a lower nucleation density when intermediate conversion, as previously reported for multi-step thermal annealing approaches.[62,63] Photoluminescence (PL) mapping across different substrate positions showed improved spatial homogeneity of emission intensity, while single-spot PL spectra exhibited reduced spectral inhomogeneity and increased intensity (Figure S5, Supporting Information). These improvements in film quality translated directly into enhanced device performance, with J–V characteristics showing increased open-circuit voltage (V_{OC}) and fill factor (FF) together with a reduced spread of the results, confirming that the gains in phase purity and spatial homogeneity are reflected at the device level (Figure S6, Supporting Information). We obtained uniform NiO_X and WBG perovskite layers with average thicknesses of approximately 14 nm and 490 nm, respectively, as derived from ellipsometry mapping (Figure S7, Supporting Information). Full processing details are provided in the Experimental Section.

To evaluate the impact of the hole-selective interlayer, identical devices were fabricated employing two different SAM molecules: TRIPOD-C4 and (4-(3,6-Dimethyl-9H-carbazol-9-yl)butyl)phosphonic acid (Me-4PACz), both prepared at equivalent molar concentrations. TRIPOD-C4 is a carbazole-based molecule with three phosphonic acid anchoring sites (Figure 1e), which promotes favourable planarization of the conjugated aromatic system - a molecular design that is particularly advantageous for solution-based deposition over large areas.[55,64] We previously reported that spin-coated WBG PSCs utilizing TRIPOD-C4 exhibit improved efficiency and enhanced phase stability compared to those using Me-4PACz. These improvements were attributed to a more uniform coverage of NiO_X, improved hole extraction, and reduced non-radiative interfacial recombination.[55] Statistics of photovoltaic parameters derived from current density-voltage (J-V) characterization of WBG PSCs with distinct SAM molecules are summarized in Table 1. The devices utilizing TRIPOD-C4 demonstrated superior performance, primarily originating from a substantial increase in the fill factor (FF), which averaged 75.6% compared to 58.0% for Me-4PACz-based devices (Figure 1f-g). The best-performing TRIPOD-C4 device delivered a PCE of 15.7%. This result extends the applicability of TRIPOD-C4 from spin-coated devices, as previously reported, to a blade-coated configuration, confirming that the multi-anchoring molecular design remains effective under scalable deposition conditions. Table 1 summarizes photovoltaic parameters extracted from the J-V measurements of blade-coated WBG PSCs with different SAM molecules.

Additionally, we subjected WBG PSCs to a bending durability test, where devices retained over 90% of their initial performance after 10,000 bending cycles at a radius of 10 mm (Figure S8, Supporting Information).

View Article Online
DOI: 10.1039/D6EL00050A

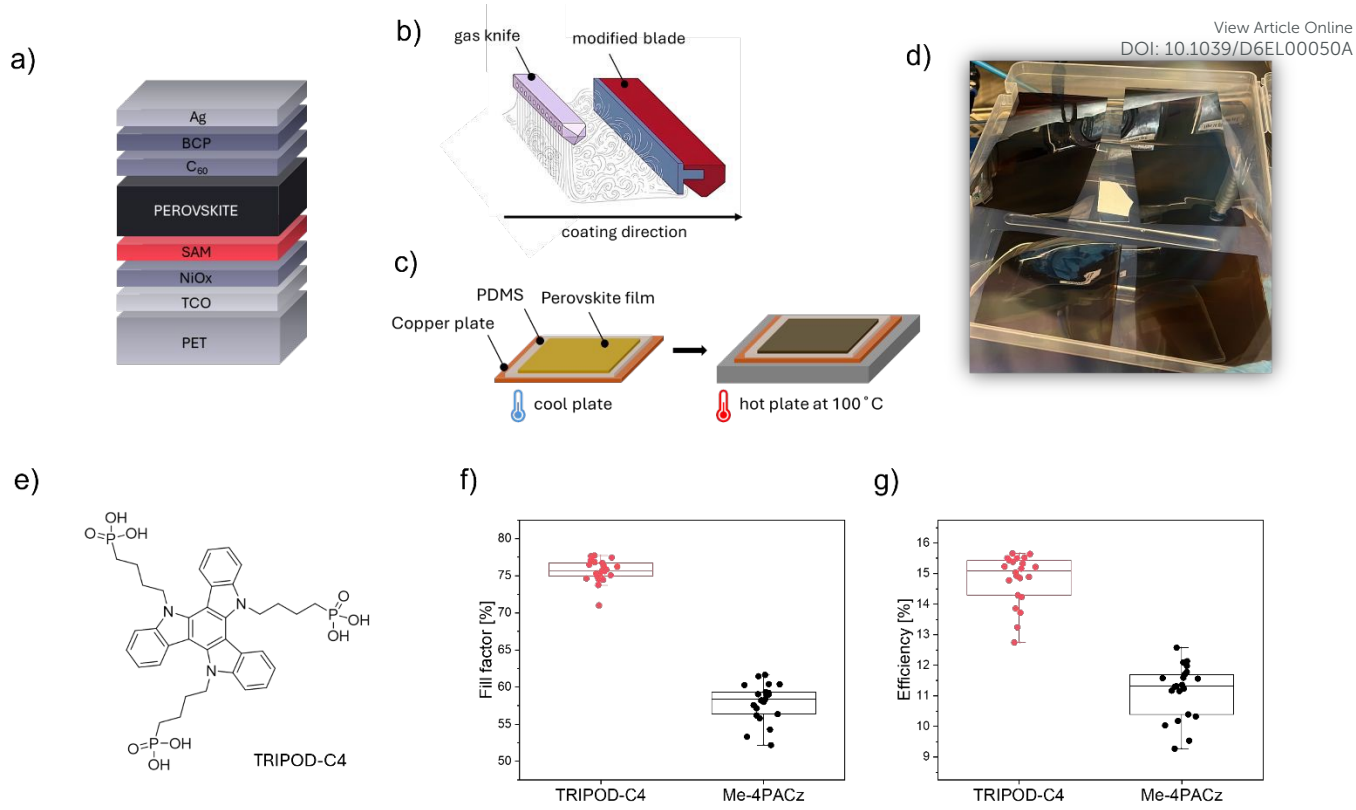

Figure 1. a) Scheme of the inverted WBG PSC layer stack, b) scheme of modified blade with a shielding element, c) scheme of gradual annealing step using PDMS-covered copper plate, d) picture of 90 cm^2-sized blade-coated samples up to perovskite from which individual solar cells were extracted, e) structure of the TRIPOD-C4, f-g) statistics of fill factor and efficiency for blade-coated WBG PSCs employing TRIPOD-C4 and Me-4PACz as a SAM.

Table 1. Summary of photovoltaic parameters extracted from the J-V measurements of blade-coated WBG PSCs with different SAM molecules.

SAM molecule	PCE (%)	FF (%)	V_{OC} (V)	J_{SC} (mA/cm^2)
TRIPOD-C4	15.7 (14.8 ± 0.8)	77.7 (75.6 ± 1.5)	1.14 (1.10 ± 0.02)	18.7 (17.8 ± 0.8)
Me-4PACz	12.6 (11.2 ± 0.9)	61.6 (58.0 ± 2.5)	1.12 (1.08 ± 0.02)	18.4 (17.7 ± 0.6)

Next, to assess the universality of the developed approach, we reduced the bromide content in the perovskite composition from 35% to 10%, while maintaining the same precursor molarity, solvent system, and additives. As a result, a medium-bandgap (MBG) perovskite with an optical bandgap of 1.61 eV was obtained (Figure S9, Supporting Information). The selection of these two compositions was motivated by their complementary relevance to the broader photovoltaic landscape: the WBG absorber (Eg ~1.76 eV) is a key component in perovskite-based tandem architectures, where the top sub-cell harvests high-energy photons while matched with the narrow bandgap absorber, whereas the MBG composition (Eg = 1.61 eV) is well-suited for single-junction applications and represents a compositional regime with markedly more controlled crystallization dynamics. A central motivation of this work was to demonstrate that a single optimized processing framework, encompassing the same solvent system, additives, layer stack, and blade-coating parameters, can yield high-quality films and efficient devices across both compositions, despite the substantially different crystallization kinetics imposed by the bromide content.

The X-ray diffractograms of WBG and MBG perovskite films revealed intense reflexes at around 14.4° and 28.9° (2θ), corresponding to the pseudocubic (100) and (200) crystallographic planes, respectively (Figure S10, Supporting Information). The WBG perovskite exhibited diffraction peaks shifted toward higher 2θ values relative to the MBG composition, consistent with lattice contraction induced by the increased bromide content. This shift arises from the smaller ionic radius of Br^- (1.96 Å) compared to I^- (2.20 Å), which results in contracted unit cell parameters and higher-angle Bragg reflections.[65] The diffractogram of the WBG perovskite composition additionally revealed a negligible peak at 12.8˚ , which corresponds to the (001) plane of

View Article Online
DOI: 10.1039/D5EE00059A

residual hexagonal lead iodide (PbI_2).[66] Consistent with this observation, top-view SEM imaging revealed trace amounts of residual PbI_2, visible as bright intrusions protruding from the film surface (Figure S4b, Supporting Information). In contrast, no PbI_2 reflection was detected in the diffractogram of the MBG perovskite film, reflecting the compositional dependence of the crystallization dynamics between the two perovskite compositions.[67,68] To further evaluate the optoelectronic quality and phase homogeneity of the two absorbers, steady-state photoluminescence (ss-PL) spectra were collected from the perovskite films prior to device completion (Figure S11, Supporting Information). Both compositions exhibit single, well-defined emission peaks with no secondary features or shoulders indicative of halide phase segregation, confirming the phase purity of both blade-coated films. Nevertheless, the MBG perovskite film exhibits approximately one order of magnitude higher PL intensity than the WBG perovskite, indicating higher optoelectronic quality, consistent with the greater susceptibility of bromide-rich compositions to trap-state formation and compositional heterogeneity during crystallization.[67,68] Taken together, the XRD and PL data confirm that, although both absorbers are phase-pure, the WBG composition exhibits inherently lower phase homogeneity than MBG composition.

Next, we fabricated MBG and WBG PSCs applying the same optimized processing conditions and TRIPOD-C4 as a SAM. To further improve device performance, the perovskite top surface was passivated with propane-1,3-diammonium iodide ($PDAI_2$). $PDAI_2$ has been reported to form a surface dipole that increases the n-type character of the perovskite surface, thereby repelling holes near the electron-transporting layer (ETL) and suppressing interfacial recombination.[69–72] The $PDAI_2$ treatment increased the ss-PL intensity and elevated the V_{OC} of both WBG and MBG devices (Figure S12-S13, Supporting Information), suggesting suppressed non-radiative recombination at the perovskite/ETL interface. The schematic of the optimized PSC layer stack is shown in Figure 2a. The blade-coated PSCs yielded average PCEs of 19.5% and 16.0% for the MBG and WBG perovskite, respectively (Figure 2b). The champion MBG PSC delivered a PCE of 20.4% (FF = 76.6%, V_{OC} = 1.17 V, J_{SC} = 22.5 mA/cm²), while the best-performing WBG PSC yielded 17.4% (FF = 80.1%, V_{OC} = 1.22 V, J_{SC} = 17.7 mA/cm²), both with negligible hysteresis (Figure 2c). The statistics of all photovoltaic parameters are listed in Table 2.

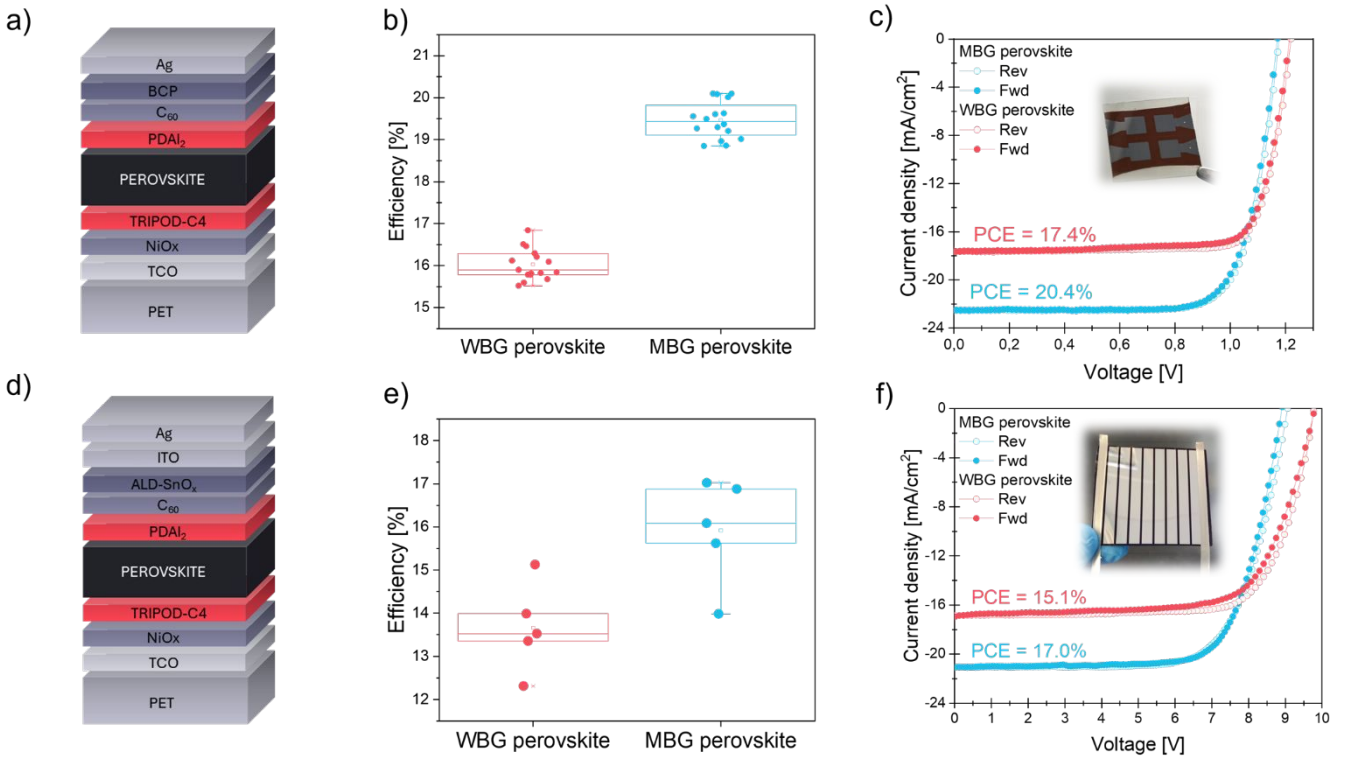

Figure 2. a) Scheme of the optimized inverted PSCs stack, b) statistics of efficiency for flexible, blade-coated solar cells employing WBG and MBG perovskite absorbers, c) J-V curves (forward and reverse scan directions) of top-performing solar cells with the WBG and MBG absorbers, d) scheme of the optimized inverted PSMs stack, e) statistics of efficiency for flexible, blade-coated solar modules employing WBG and MBG perovskite absorbers, f) J-V curves (forward and reverse scan directions) of top-performing solar module with the WBG and MBG perovskite absorbers

Table 2. Summary of photovoltaic parameters extracted from the J-V measurements of blade-coated solar cells and modules with WBG and MBG perovskite absorbers.

View Article Online
DOI: 10.1039/D6EL00050A

Device type	PCE (%)	FF (%)	V_{OC} (V)	J_{SC} (mA/cm^2)
WBG PSCs	17.4 (16.0 ± 0.4)	80.1 (75.2 ± 2.0)	1.22 (1.19 ± 0.02)	17.7 (17.7 ± 0.3)
WBG PSMs	15.1 (13.7 ± 1.0)	73.8 (68.0 ± 5.3)	9.78 (9.65 ± 0.09)	17.4 (16.8 ± 0.6)
MBG PSCs	20.4 (19.5 ± 0.4)	76.6 (75.5 ± 2.0)	1.17 (1.14 ± 0.02)	22.5 (22.4 ± 0.2)
MBG PSMs	17.0 (15.9 ± 1.2)	72.5 (69.2 ± 4.9)	8.98 (8.87 ± 0.10)	21.5 (20.7 ± 0.5)

Figure S14 in Supporting Information presents an overview of the most recent reported PSCs fabricated using scalable techniques on both rigid and flexible substrates, categorized by perovskite bandgap. The data clearly demonstrate that devices processed on flexible substrates exhibit lower performance and represent a minority of the reported work. Similarly, the fabrication of flexible modules using scalable methods remains limited. This scarcity is particularly evident for wide-bandgap compositions (Eg ≥ 1.7 eV) on flexible substrates, where few reports employing scalable deposition methods are available. The present work contributes to this underexplored area by demonstrating efficient blade-coated devices at both 1.61 eV and 1.76 eV using a unified processing framework.

Solar modules blade-coating

We leveraged our optimized architecture and blade-coating process to fabricate perovskite solar modules (PSMs). For the module stack, BCP was replaced with the tin oxide deposited by atomic layer deposition (ALD-SnO_X) to enhance device stability. At elevated temperatures, BCP is prone to morphological degradation, leading to interface deterioration and performance loss.[73,74] In contrast, a dense, conformal ALD-grown inorganic layer provides an effective diffusion barrier, retarding thermally and humidity-driven degradation pathways.[74,75] Additionally, an ITO layer was introduced between ALD-SnO_X and Ag electrode to prevent silver ions migration and silver electrode degradation caused by halide ions from the perovskite layer, which often leads to device failure.[76] The schematic of the module layer stack is shown in Figure 2d.

We fabricated 8-cell modules with an active area of 15.2 cm^2. The WBG PSMs yielded an average PCE of 13.7%, whereas the MBG PSMs delivered 15.9% (Figure 2e). The best-performing WBG module achieved PCE of 15.1% (FF = 73.9%, V_{OC} = 9.77 V, J_{SC} = 16.9 mA/cm^2) and the champion MBG module yielded 17.0% (FF = 73.1%, V_{OC} = 8.84 V, J_{SC} = 21.1 mA/cm^2), both with a negligible hysteresis (Figure 2f). The statistics of all photovoltaic parameters extracted from the modules' J-V measurements are listed in Table 2. Table S1, Supporting Information summarizes the state-of-the-art inverted PSCs and PSMs fabricated using scalable deposition methods on polymeric foils. The data reveal a cell-to-module PCE loss, which could be attributed to increased area and/or interconnection losses. Notably, the results achieved in this work represent some of the highest reported PCE values, with the lowest cell-to-module loss. The WBG module is of particular interest for use as a sub-cell in flexible all-perovskite tandem architectures. Notably, reports on scalable fabrication of inverted flexible modules employing WBG FA–Cs perovskite absorbers (Eg≥1.7 eV) remain limited, highlighting the relevance of these results for the development of future flexible tandem devices.

Solar modules lamination and stability testing

Next, the MBG perovskite modules were vacuum-laminated with foils of ultra-high barrier properties to preserve their inherent light weight and facilitate large-scale processing. Conventional silicon PV (Si-PV) encapsulation protocols are not directly transferable to perovskite PV devices due to their higher thermochemical sensitivity. Encouraging damp-heat stability has recently been demonstrated for flexible perovskite solar modules encapsulated with high-barrier foils.[77–79] However, the reported encapsulation architectures frequently rely on wide lateral margins rather than a dedicated edge sealant, thereby constraining the achievable aperture-to-total-area ratio and limiting compatibility with high-throughput manufacturing. The incorporation of a dedicated edge sealant alongside vacuum lamination, a process well-established in conventional silicon PV manufacturing, not only improves the aperture-to-total-area ratio but also mitigates the risk of residual gas entrapment. Nevertheless, reports on combining industrially scalable vacuum lamination, a dedicated edge sealant, and ultra-barrier foils for flexible perovskite modules remain exceptionally scarce in the literature. The encapsulation sequence reported here is therefore of practical significance, as it demonstrates the feasibility of adapting the established silicon PV lamination method to flexible perovskite modules while maintaining the mechanical compliance and low thermal budget required by polymeric substrates.

Here, the MBG PSMs were encapsulated with a commercial barrier foil, using a thermoplastic polyolefin (TPO) encapsulant adhesive. Both the barrier foil and the encapsulant film had thicknesses on the order of 200 µm and were applied symmetrically

View Article Online
DOI: 10.1039/D5EL00050A

on both sides of the device. The edges were sealed with a polymer-based polyisobutylene edge-sealant. The use of a dedicated perimeter seal, rather than wide lateral encapsulant margins, supports a more favourable aperture-to-total-area ratio of the laminated module. Electrical interconnection to the external circuit was realized via a current-collector tape. The schematic of the employed encapsulation layer stack is shown in Figure 3a.

Si-PV modules are typically vacuum-laminated at 135–150 °C under high vacuum, conditions that are not compatible with PSMs fabricated on PET foils.[75] Here, the vacuum lamination was performed at 120 °C with the pressure step omitted. To ensure reliable sealing between the edge-seal material and the barrier foils, the lamination was followed by a supplementary heated pressing step applied along the perimeter of the lamination stack. A picture of the encapsulated MBG PSM is shown in Figure 3b. The PV parameters extracted from I-V curves of laminated modules are provided in Table S2, Supporting Information. The best-performing laminated MBG PSM delivered a PCE of 14.8% from the J-V scan (14.6% from maximum power point tracking (MPPT)). The WBG PSMs were not encapsulated in this study, as their target application is integration as a sub-cell in an all-perovskite tandem architecture. In such a configuration, the layer stack introduces additional thermo-mechanical constraints and distinct moisture ingress pathways that differ substantially from those of a single-junction package.[80,81] The encapsulated modules were subjected to an accelerated damp-heat stability test (ISOS-D3) at 85 °C and 85% relative humidity. The most resilient module maintained 80% of its initial performance over a 1026-hour test duration (Figure 3c). Performance declined rapidly within the initial 66 hours, driven by a simultaneous increase in R_S and decrease in R_{SH}, as shown in Figure 3d–e. Interestingly, after the initial 66-hour period, performance partially recovered, accompanied by a reduction in R_S. In contrast, R_{SH} showed a consistent, gradual decline throughout the entire test. The four remaining modules followed similar R_S and R_{SH} trends; however, a more pronounced increase in R_S and a steeper drop in R_{SH} led to their comparatively lower final stability. The PCE recovery after the initial dip at 66 h suggests that the early performance loss is unlikely to originate from irreversible chemical degradation of perovskite material. Instead, it is consistent with thermo-mechanical stress arising from a mismatch in thermal expansion coefficients or the release of frozen strain in plastic foils within the encapsulation stack.

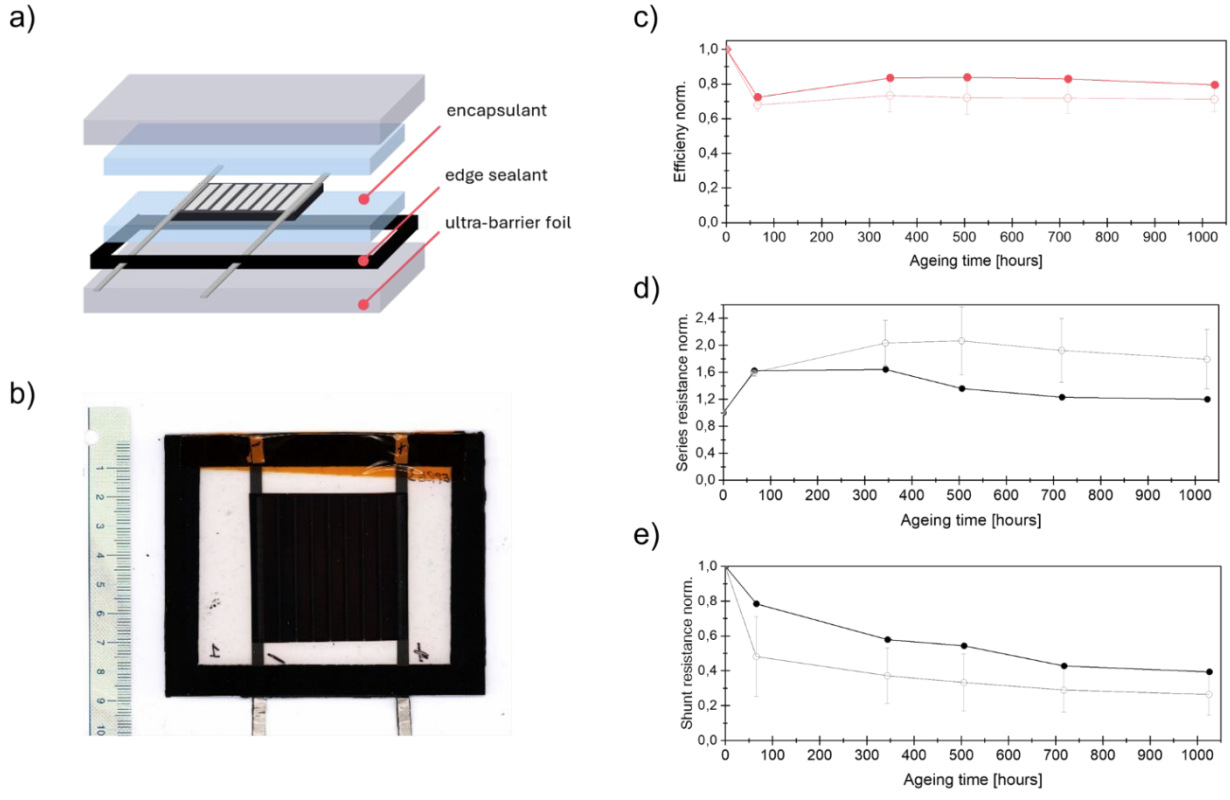

Figure 3. a) Schematic of the encapsulation layer stack, b) picture of encapsulated PSM, c) normalized efficiency evolution upon the DH stability test, d) normalized series resistance evolution upon the DH stability test, e) normalized shunt resistance evolution upon the DH stability test. On the graphs, the solid symbol represents the data for the most stable module, and open symbols represent the average and associated standard deviations across all five tested modules.

To complement the charge extraction and optoelectronic quality of the perovskite absorber, spatially resolved characterization, encompassing PL mapping under open and short-circuit conditions (PL_{OC}, PL_{SC}) was carried out (Figure S15-S16, Supporting

View Article Online
DOI: 10.1039/D5EL00050A

Information). To investigate the spatial evolution of carrier extraction during the DH test, we calculated the extraction coefficient (EC) maps from PL_{OC} and PL_{SC} images, defined as EC= ((PL_{OC} − PL_{SC})/PL_{OC})x100%.(Figure S17, Supporting Information). Horizontal line profiles were extracted at selected positions to evaluate the EC distribution across the cell stripes (Figure 4). At 0 h, the EC profiles exhibited a flat, square shape within each stripe (~80–85%), with sharp transitions at the stripe boundaries, and full spatial homogeneity, as confirmed by overlapping profiles at different y-positions. After 66 h, the EC dropped uniformly across the full stripe width to approximately 65–73%, consistent with the concurrent R_S increase derived from I–V measurements and indicating a homogeneous degradation of carrier extraction across the active area of the module. At 180 h, as R_S partially recovered, the EC level also increased; however, the stripe edges recovered more rapidly than the centres, resulting in a U-shaped profile. From 506 h onward, the EC profile inverted: the edges exhibited lower EC than the centers, yielding a dome-shaped distribution that was maintained through 1026 h, with central EC values of approximately 80–86%. This inversion occurred during the period when the monotonic R_{SH} decline became the dominant driver of PCE loss, suggesting a distinct degradation mechanism. In parallel, the absolute PL_{OC} signal decreased progressively over the test duration (Figure S15). At the end of the aging test the EC remained relatively preserved but with reduced homogeneity. The PL_{OC} reduction reflects degradation of the optoelectronic quality of the perovskite absorber, consistent with the formation of PbI_2, as confirmed by XRD of the aged module (Figure S18, Supporting Information).

Taken together, the EC analysis reveals three distinct stages: (i) a uniform EC reduction at 66 h, concurrent with the R_S increase, suggesting a homogeneous process across each stripe; (ii) a spatially non-uniform recovery (180–343 h), with faster extraction recovery at stripe edges, indicating position-dependent kinetics; and (iii) a progressive EC profile inversion from 506 h onward, correlating with dominant R_{SH} decline and absorber degradation. We attribute the initial uniform EC drop to thermo-mechanical stress originating from the encapsulation stack, causing partial loss of interfacial contact, an effect absent in unencapsulated modules aged at the same temperature in an inert atmosphere (Figure S19, Supporting Information). The observed performance degradation mode highlights the dual role of the encapsulation stack, which must simultaneously provide an effective moisture barrier without inducing deleterious mechanical stress within the device.

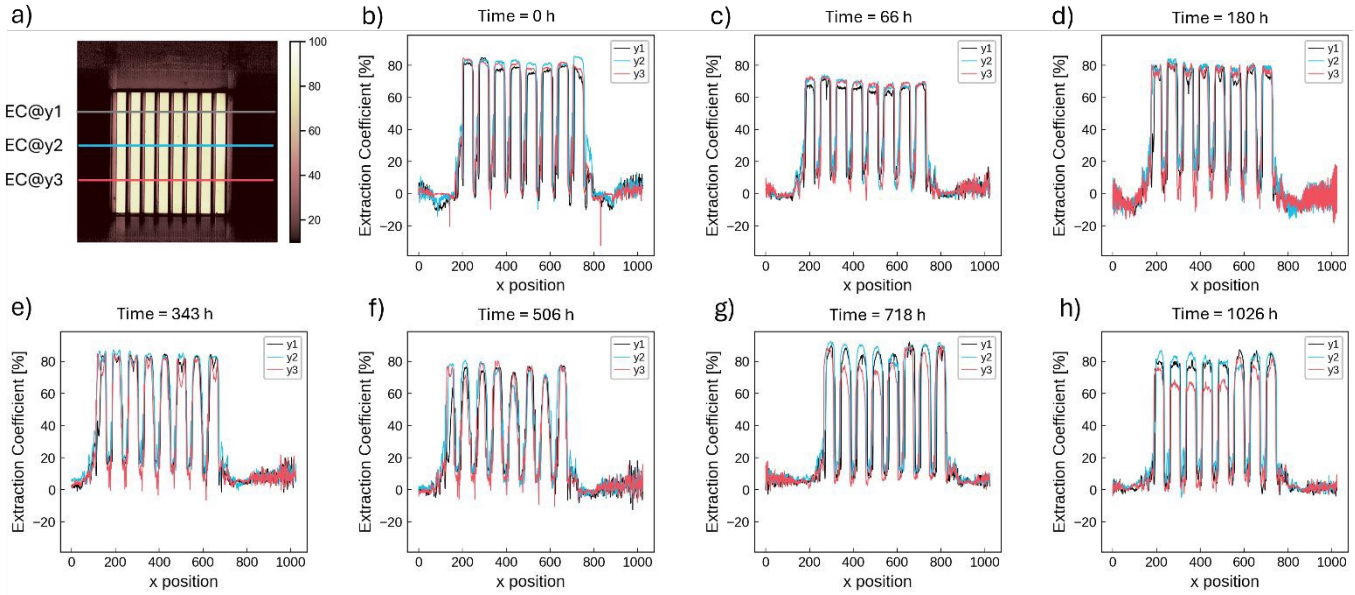

Figure 4. Spatially resolved extraction coefficient analysis of the most stable module at all measured time points during the DH test. a) illustration of the line profile extraction methodology: map of extraction coefficient of the module with the indicated positions of three horizontal line scans (z@y1, z@y2, z@y3), b–h) extraction coefficient profiles along the x-direction recorded at three y-positions at b) 0 h, c) 66 h, d) 180 h, e) 343 h, f) 506 h, g) 718 h, and h) 1026 h of the DH test.

Conclusions

In this work, we have demonstrated the fabrication and lamination of inverted perovskite PV devices using scalable techniques and methodology suitable for polymeric substrates. Interface engineering, employing TRIPOD-C4 as a SAM and $PDAI_2$ to passivate the perovskite/ETL interface, enabled blade-coated FA–Cs PSCs with bandgaps of 1.61 eV and 1.76 eV to reach PCEs of 20.4% and 17.4%, respectively. The optimized layer stack and fabrication process were successfully transferred to large-area module manufacturing, achieving champion efficiencies of 17.0% (E_g = 1.61 eV) and 15.1% (E_g = 1.76 eV). Furthermore, the laminated modules exhibited robust environmental stability, retaining up to 80% of their initial performance after 1026 hours of damp heat

View Article Online DOI: 10.1039/D5EE00870A

testing (ISOS-D3, 85°C, 85% RH). This stability result, achieved with a production-compatible vacuum lamination protocol on a flexible substrate, represents an encouraging step towards meeting the durability requirements of commercially viable flexible perovskite PV. We have demonstrated that a single optimized blade-coating framework, incorporating a shielding element for controlled intermediate-phase formation and a gradual annealing protocol compatible with thermally sensitive PET substrates, can yield efficient devices and modules across FA–Cs perovskite compositions with bandgaps of 1.61 eV and 1.76 eV, despite the markedly different crystallization dynamics imposed by the bromide content. The synergistic interface engineering approach, employing TRIPOD-C4 and $PDAI_2$, proved effective for efficiency improvement under scalable deposition conditions. Taken together, this work provides an integrated demonstration of the scalable fabrication and environmental validation of flexible FA-Cs perovskite solar modules. The methodology presented in this work, from blade-coating on free-standing PET foils, through vacuum lamination, to ISOS-D3 stability testing, establishes a scalable processing route compatible with large-scale manufacturing. We anticipate that the insights into the degradation modes of flexible modules under damp heat conditions will facilitate the optimisation of encapsulation architectures, thereby advancing the long-term reliability of flexible perovskite photovoltaic devices toward commercial deployment.

Experimental section

Materials

Unless otherwise stated, all the materials were purchased and used as received. Indium tin oxide (ITO)-coated polyethylene terephthalate (PET) substrates (sheet resistance of 60 Ω/□) were bought from Eastman Chemical Company. Lead iodide (PbI_2, 99.99%), cesium bromide (CsBr, 99.9%), [4-(3,6-Dimethyl-9H-carbazol-9-yl)butyl]phosphonic acid (Me-4PACz, >99.0%) were purchased from Tokyo Chemical Industry Co. Ltd. Lead bromide ($PbBr_2$, 98%), cesium iodide (CsI, 99.9%), fullerene-C_{60} (C_{60}, 99.9%), bathocuproine (BCP, 99.99%), lead thiocyanate, ($Pb(SCN)_2$, 99.5%) were purchased from Sigma Aldrich. Formamidinium iodide (FAI, 99%) was obtained from Ajay North America, and formamidinium bromide (FABr, 99.99%) from Dyenamo. 4-Fluorophenethylammonium iodide (4FPEAI) and propane-1,3-diammonium iodide ($PDAI_2$, >98.0%) were bought from GreatCell Solar. N-metylopirolidon anhydrous (NMP, 99.5%), N, N-dimethylformamide anhydrous (DMF, 99.8%), dimethyl sulfoxide (DMSO, 99.9%), and 2-Propanol (IPA, 99.9%) were purchased from Sigma Aldrich. Ethanol (EtOH, 99.8%) was bought from ChemPur. Silver pellets (Ag, 99.99%) and indium-tin oxide target (ITO, 99.99%) were purchased from Kurt. J. Lesker. TRIPOD-C4 was synthesized using a previously reported method.[55] NiO_x was synthesized internally, following the procedure described in the Supporting Information.

Perovskite precursor preparation

The WBG perovskite precursor solution (nominal perovskite composition: $Cs_{0.2}FA_{0.8}Pb(I_{0.65}Br_{0.35})_3$) was prepared with a molarity of 1.15 M, following the recipe: 0.15 mmol of CsI, 0.08 mmol of CsBr, 0.6 mmol of FAI, 0.32 mmol of FABr, 0.4 mmol of $PbBr_2$, and 0.75 mmol of PbI_2, dissolved in 1 mL of DMF:NMP (9:1, v/v). Solution was continuously stirred overnight at around 20°C. After overnight stirring, the additives were dissolved in the perovskite precursor solution. The molarities of the additives were 1.5 mol% with respect to perovskite (4FPEAI) and 2 mol% $Pb(SCN)_2$. The solution was left to dissolve for 1-2 hours without stirring. The precursor solution was filtered with a 0.22 µm polytetrafluoroethylene (PTFE) membrane before use. The MBG perovskite precursor solution (nominal perovskite composition: $Cs_{0.2}FA_{0.8}Pb(I_{0.90}Br_{0.10})_3$) was prepared with a molarity of 1.15 M, following the same recipe and procedure as for WBG perovskite precursor but with reduced bromide fraction: 0.20 mmol of CsI, 0.02 mmol of CsBr, 0.8 mmol of FAI, 0.09 mmol of FABr, 0.12 mmol of $PbBr_2$, and 1.1 mmol of PbI_2.

Device fabrication

Perovskite solar cells and modules were fabricated in a p-i-n architecture. A blade-coater from Erichsen and an applicator from Zehntner were used for blade-coating. The substrates were planarized for deposition by applying IPA beneath the substrate to promote capillary-assisted seating on the platen. To fabricate the devices, a PET-ITO substrate measuring 18.5 x 29.0 cm was patterned with a near-infrared laser (1064 nm) to delineate the device design (cell or module). This large-area laser-patterned substrate was subsequently used to blade-coat NiO_X and SAM layers. Following the laser patterning, the substrate was cleaned using isopropanol, dried with nitrogen gas, and exposed to oxygen plasma for 2 minutes. The NiO_X powder was kept in a dry and inert atmosphere, and the Milli-Q water was kept refrigerated. The NiO_X dispersion was prepared by dissolving 20 mg of NiO_X powder in 1 mL of cold Milli-Q water, which was then sonicated for 5 minutes in a cold water bath. Finally, the dispersion was filtered through a 0.45 µm PTFE membrane prior to deposition. 350 µL of NiO_X dispersion was blade-coated in a clean-room environment using with a blade gap set at 450 µm height and a 2.5 mm/s speed, followed by annealing at 100°C for 30 minutes in the oven. After NiO_X deposition, the substrate was transferred to a nitrogen-filled glovebox for SAM and perovskite layer deposition. The Me-4PACz solution was prepared inside a nitrogen-filled glovebox by dissolution of 1mmol of Me-4PACz in 1mL of ethanol. The TRIPOD-C4 solution was prepared inside a nitrogen-filled glovebox by dissolution of 1mmol of powder in 1 mL of DMF. The TRIPOD-C4 solution was stirred overnight and filtered just before deposition with a polyvinylidene fluoride (PVDF) 0.45 µm filter. The SAM (TRIPOD-C4 or Me-4PACz) solution was blade-coated twice on the NiO_X layer in opposite directions. For each deposition, 800 µL of solution was applied using a blade with a 400 µm gap and a speed of 2.5 mm/s, followed by annealing at 100°C for 10 minutes on a hotplate inside the glovebox. After SAM deposition, the 18.5 x 29.0 cm substrate was sectioned into six

View Article Online
DOI: 10.1039/D5EY00059A

equal pieces, each about 90 cm², for deposition of the perovskite layer. The blade-coating procedure was the same for WBG and MBG perovskite absorbers. 120 µL of solution was applied using a blade gap set to 400 µm height and a speed of 3.5 mm/s, with nitrogen quenching. To promote solvent removal, gas quenching with nitrogen at 2.5 bar was applied perpendicular to the substrate using an air knife. The gas flow was terminated immediately after the pass. After a 20–30 s wait, the sample was placed on a PDMS-covered, room-temperature copper plate and transferred to a hotplate set at 100 °C for 30 min. After cooling down, the perovskite surface was passivated with $PDAI_2$. The $PDAI_2$ solution was prepared in a nitrogen-filled glovebox by dissolving 2 mg of powder in 1 mL of IPA. 100 µL of solution was applied using a blade gap set to 400 µm in height and a deposition speed of 10 mm/s, assisted by nitrogen at 1 bar. The sample was annealed at 100°C for 10 minutes. Next, the 30 nm of fullerene C_{60} was deposited as an electron-transporting layer, using thermal evaporation at ~10^{-6} mbar. In the case of solar cells, 5 nm of BCP buffer layer and 110 nm of Ag electrode were deposited by thermal evaporation at ~10^{-6} mbar. The metal electrode was deposited through a shadow mask, resulting in an active area of 0.1 cm². For the modules, deposition of C_{60} was followed by a 10 nm-thick tin oxide layer via atomic layer deposition (ALD-SnO_x). The ALD-SnO_x process conditions follow a previously published procedure[82]. Then, the laser ablation step was performed through the stack down to the TCO to create the series interconnection (P2). Finally, 40 nm ITO and 110 nm Ag were sputtered through a shadow mask (P3) to form the top electrode. The ITO sputtering details follow a previously published procedure.[82] The module consisted of 8-cell modules connected in series, resulting in an active area of 15.2 cm² and a total area of 25 cm² (GFF 60.3%).

Modules encapsulation

Vacuum lamination was performed using commercial barrier foil with WVTR <1x10^{-4} gm^{-2} day^{-1} (at 38°C/90% RH) using a TPO-based lamination encapsulant. A barrier foil and an encapsulant film (each around 200 µm thick) were applied to both sides of the device stack. The lamination process was conducted under vacuum (<50 mbar) at 120°C; the conventional pressure step applied after the vacuum step was omitted. The total residence time in the laminator was 480 s. The device perimeter was sealed with a polybutylene-based edge-seal tape (10 mm width, 0.6 mm thickness). To ensure proper sealing between the edge-seal material and the barrier foils, the lamination was followed by an additional heated pressing step applied to the package sides. External contacts were formed using a current-collector tape (4 mm width, 60 µm thickness).

Author contributions

A.W.M.: conceptualization, data curation, formal analysis, methodology, investigation, validation, visualization, writing – original draft, writing – review & editing; M.Ś.: data curation, formal analysis, methodology, validation, visualization, writing – review & editing; K.B.: data curation, formal analysis, methodology, validation, investigation, visualization, writing – review & editing; D.R.M.: methodology, data curation, validation, visualization, writing – review & editing; Ł.P.: methodology, writing – review & editing; K.D.: data curation, methodology, writing – review & editing; P.J.: methodology; K.R.: methodology; D.T.: data curation, formal analysis, methodology, writing – review & editing; A.D.C.: supervision, writing – review & editing; K.W.: supervision, project administration, funding acquisition, writing – review & editing.

Conflicts of interest

There are no conflicts to declare.

Data availability

The supporting data has been provided as part of the Supplementary Information.

Acknowledgements

This work was part-funded by the National Science Center as part of the “OPUS LAP” cooperation (PALACE project, grant no: 2021/43/I/ST5/03245), the National Center for Research and Development (grant no: LIDER13/0217/2022), and the European Union’s Horizon Europe research and innovation program (Supertandem project, grant no. 101075605). A.D.C. and D.T. acknowledge the European Union’s Horizon Europe research and innovation program under grant agreement (PEARL project, no. 101122283).

Notes and references

1 M. A. Green, A. Ho-Baillie and H. J. Snaith, *Nature Photon*, 2014, 8, 506–514.

2 L. Zhang, M. Zhang, H. Wang, Z. Li, Z. Zhang, Y. Song, X. Song, S. Wang, J. Chen, W. Li, H. Dong, F. Wang, Y. Liu, X. Li, J. Yuan, W. Ma, Y. Zhang, S. (Frank) Liu, F. Gao, Z. Wu, Z. Yang, F. Hao, K. Zhao, Z. Jin, K. Yan, J. Chang, J. Cao, J. Wang, X. Zhang, Q. Dong, P. Gao, Y. Zhao, L. Xiao, Y. Ding and L. Ding, *Advanced Materials*, 2026, 38, e12221.

3 Best Research-Cell Efficiency Chart | Photovoltaic Research | NLR, https://www.nrel.gov/pv/cell-efficiency, (accessed 24 January 2026).

4 L. Zhang, L. Mei, K. Wang, Y. Lv, S. Zhang, Y. Lian, X. Liu, Z. Ma, G. Xiao, Q. Liu, S. Zhai, S. Zhang, G. Liu, L. Yuan, B. Guo, Z. Chen, K. Wei, A. Liu, S. Yue, G. Niu, X. Pan, J. Sun, Y. Hua, W.-Q. Wu, D. Di, B. Zhao, J. Tian, Z. Wang, Y. Yang, L. Chu, M. Yuan, H. Zeng, H.-L. Yip, K. Yan, W. Xu, L. Zhu, W. Zhang, G. Xing, F. Gao and L. Ding, *Nano-Micro Lett.*, 2023, 15, 177.

5 M. D. Bastiani, V. Larini, R. Montecucco and G. Grancini, *Energy & Environmental Science*, 2023, 16, 421–429.

6 K. J. Prince, H. M. Mirletz, E. A. Gaulding, L. M. Wheeler, R. A. Kerner, X. Zheng, L. T. Schelhas, P. Tracy, C. A. Wolden, J. J. Berry, S. Ovaitt, T. M. Barnes and J. M. Luther, *Nat. Mater.*, 2025, 24, 22–33.

7 H. S. Jung and N.-G. Park, *Small*, 2015, 11, 10–25.

8 L. A. Castriotta, M. A. Uddin, H. Jiao and J. Huang, *Advanced Materials*, 2025, 37, 2408036.

9 B. Kang and F. Yan, *Energy Environ. Sci.*, 2025, 18, 3917–3954.

10 A. Khorasani, F. Mohamadkhani, M. Marandi, H. Luo and M. Abdi-Jalebi, *Advanced Energy and Sustainability Research*, 2024, 5, 2300275.

11 A. Agresti, F. Di Giacomo, S. Pescetelli and A. Di Carlo, *Nano Energy*, 2024, 122, 109317.

12 M. J. M. Marques, W. Lin, T. Taima, S. Umezu and Md. Shahiduzzaman, *Materials Today*, 2024, 78, 112–141.

13 H.-C. Cha, S.-H. Huang, C.-F. Li, F.-Y. Tsai, W.-F. Su and Y.-C. Huang, *Sustainable Energy Fuels*, 2025, 9, 5962–6006.

14 H. Zhong, Y. Wang, L. Hou, X. Song and F. Zhang, *ACS Appl. Mater. Interfaces*, 2025, 17, 50168–50190.

15 V. Romano, A. Agresti, R. Verduci and G. D'Angelo, *ACS Energy Lett.*, 2022, 7, 2490–2514.

16 A. Grabowska, R. Fuentes Pineda, P. Spinelli, G. Soto Pérez, F. A. Vinocour Pacheco and V. Babu, *ACS Appl. Mater. Interfaces*, 2024, 16, 48676–48684.

17 K. Wojciechowski, D. Forgács and T. Rivera, *Solar RRL*, 2019, 3, 1900144.

18 B. Hailegnaw, S. Demchyshyn, C. Putz, L. E. Lehner, F. Mayr, D. Schiller, R. Pruckner, M. Cobet, D. Ziss, T. M. Krieger, A. Rastelli, N. S. Sariciftci, M. C. Scharber and M. Kaltenbrunner, *Nat Energy*, 2024, 9, 677–690.

19 S. Aftab, G. Koyyada, Z. Ali, M. A. Assiri, J. H. Kim, N. Rubab and E. Akman, *Materials Today Energy*, 2025, 51, 101872.

20 A. S. R. Bati, Y. L. Zhong, P. L. Burn, M. K. Nazeeruddin, P. E. Shaw and M. Batmunkh, *Commun Mater*, 2023, 4, 2.

21 R. Yin, Y. Wu, Z. Huang, A. S. Vasenko, S. Xu and H. Zhou, *Advanced Functional Materials*, 2025, 35, 2419184.

22 N.-G. Park and K. Zhu, *Nat Rev Mater*, 2020, 5, 333–350.

23 J. L. Starger, A. E. Louks, K. Schutt, E. A. Gaulding, R. W. Epps, R. C. Bramante, R. A. Kerner, K. Zhu, J. J. Berry, N. J. Alvarez, R. A. Cairncross and A. F. Palmstrom, *Cell Reports Physical Science*, 2025, 6, 102655.

24 S. Ternes, F. Laufer and U. W. Paetzold, *Advanced Science*, 2024, 11, 2308901.

25 Z. Jiang, F. Ren, Q. Zhou, B. Wang, Z. Sun, M. Li, Z. Zhao, Z. Liu and W. Chen, *Advanced Energy Materials*, 2025, 15, 2500598.

26 C. Dong, G. Chen, F. Yao, Z. Yu, K. Dong, S. Du, L. Huang, C. Wang, T. Wang, S. Wang, W. Ke and G. Fang, *Advanced Optical Materials*, 2025, 13, 2401955.

27 J. Yang, D. K. LaFollette, B. J. Lawrie, A. V. Ievlev, Y. Liu, K. P. Kelley, S. V. Kalinin, J.-P. Correa-Baena and M. Ahmadi, *Advanced Energy Materials*, 2023, 13, 2202880.

28 X. Jia, K. Zhang, X. Gao, X. Liao, Y. Yang, W. Li, X. Lv, X. Zhao, J. Liu, Y. Ji, Z. Yan, Q. Du, F. Huang, Z. Ren, Y. Zhai, W. Huang, Y. Bai, C. Yao, Q. Lin, Y.-B. Cheng and J. Tong, *Science Advances*, 2025, 11, eadv4501.

29 Y. An, N. Zhang, Z. Zeng, Y. Cai, W. Jiang, F. Qi, L. Ke, F. R. Lin, S.-W. Tsang, T. Shi, A. K.-Y. Jen and H.-L. Yip, *Advanced Materials*, 2024, 36, 2306568.

30 R. Wang, X. Liu, S. Yan, N. Meng, X. Zhao, Y. Chen, H. Li, S. M. H. Qaid, S. Yang, M. Yuan and T. He, *Nat Commun*, 2024, 15, 8899.

31 Q. Wali, I. E. Lee, M. Aamir, T. C. Chuah and R. Jose, *Surfaces and Interfaces*, 2025, 76, 107922.

32 H. Liang, W. Yang, J. Xia, H. Gu, X. Meng, G. Yang, Y. Fu, B. Wang, H. Cai, Y. Chen, S. Yang and C. Liang, *Advanced Science*, 2023, 10, 2304733.

33 S. Ma, G. Yuan, Y. Zhang, N. Yang, Y. Li and Q. Chen, *Energy Environ. Sci.*, 2022, 15, 13–55.

34 Q.-Q. Chu, Z. Sun, D. Wang, B. Cheng, H. Wang, C.-P. Wong and B. Fang, *Matter*, 2023, 6, 3838–3863.

35 P. Mariani, M. Á. Molina-García, J. Barichello, M. I. Zappia, E. Magliano, L. A. Castriotta, L. Gabatel, S. B. Thorat, A. E. Del Rio Castillo, F. Drago, E. Leonardi, S. Pescetelli, L. Vesce, F. Di Giacomo, F. Matteocci, A. Agresti, N. De Giorgi, S. Bellani, A. Di Carlo and F. Bonaccorso, *Nat Commun*, 2024, 15, 4552.

36 Y. Wang, I. Ahmad, T. Leung, J. Lin, W. Chen, F. Liu, A. M. C. Ng, Y. Zhang and A. B. Djurišić, *ACS Mater. Au*, 2022, 2, 215–236.

37 T. Ahmad, S. Dasgupta, S. Almosni, A. Dudkowiak and K. Wojciechowski, *ENERGY & ENVIRONMENTAL MATERIALS*, 2023, 6, e12434.

38 L. Mu, S. Wang, H. Liu, W. Li, L. Zhu, H. Wang and H. Chen, *Advanced Functional Materials*, 2025, 35, 2415353.

39 M. V. Khenkin, E. A. Katz, A. Abate, G. Bardizza, J. J. Berry, C. Brabec, F. Brunetti, V. Bulović, Q. Burlingame, A. Di Carlo, R. Cheacharoen, Y.-B. Cheng, A. Colsmann, S. Cros, K. Domanski, M. Dusza, C. J. Fell, S. R. Forrest, Y. Galagan, D. Di Girolamo, M. Grätzel, A. Hagfeldt, E. von Hauff, H. Hoppe, J. Kettle, H. Köbler, M. S. Leite, S. (Frank) Liu, Y.-L. Loo, J. M. Luther, C.-Q. Ma, M. Madsen, M. Manceau, M. Matheron, M. McGehee, R. Meitzner, M. K. Nazeeruddin, A. F. Nogueira, Ç. Odabaşı, A. Osherov, N.-G. Park, M. O. Reese, F. De Rossi, M. Saliba, U. S. Schubert, H. J. Snaith, S. D. Stranks, W. Tress, P. A. Troshin, V. Turkovic, S. Veenstra, I. Visoly-Fisher, A. Walsh, T. Watson, H. Xie, R. Yıldırım, S. M. Zakeeruddin, K. Zhu and M. Lira-Cantu, *Nat Energy*, 2020, 5, 35–49.

40 D. Zhang, D. Li, Y. Hu, A. Mei and H. Han, *Commun Mater*, 2022, 3, 58.

41 H. Zhu, S. Teale, M. N. Lintangpradipto, S. Mahesh, B. Chen, M. D. McGehee, E. H. Sargent and O. M. Bakr, *Nat Rev Mater*, 2023, 8, 569–586.

42 Q. Emery, M. Remec, G. Paramasivam, S. Janke, J. Dagar, C. Ulbrich, R. Schlatmann, B. Stannowski, E. Unger and M. Khenkin, *ACS Appl. Mater. Interfaces*, 2022, 14, 5159–5167.
43 Ł. Haryński, K. Trocki, S. Bykkam, G. del Pozo, B. Romero, B. Bochentyn and D. Glowienka, *Solar Energy*, 2026, 303, 114131.
44 O. K. Segbefia, A. G. Imenes and T. O. Sætre, *Solar Energy*, 2021, 224, 889–906.
45 M. Knausz, G. Oreski, M. Schmidt, P. Guttmann, K. Berger, Y. Voronko, G. Eder, T. Koch and G. Pinter, *Polymer Testing*, 2015, 44, 160–167.
46 R. Cheacharoen, N. Rolston, D. Harwood, K. A. Bush, R. H. Dauskardt and M. D. McGehee, *Energy & Environmental Science*, 2018, 11, 144–150.
47 X. Zhang, S. Wu, H. Zhang, A. K. Y. Jen, Y. Zhan and J. Chu, *Nat. Photon.*, 2024, 18, 1243–1253.
48 Q. Jiang and K. Zhu, *Nat Rev Mater*, 2024, 9, 399–419.
49 W. Xu, B. Chen, Z. Zhang, Y. Liu, Y. Xian, X. Wang, Z. Shi, H. Gu, C. Fei, N. Li, M. A. Uddin, H. Zhang, L. Dou, Y. Yan and J. Huang, *Nat. Photon.*, 2024, 18, 379–387.
50 C. Gong, C. Wang, X. Meng, B. Fan, Z. Xing, S. Shi, T. Hu, Z. Huang, X. Hu and Y. Chen, *Advanced Materials*, 2024, 36, 2405572.
51 B. Fan, J. Xiong, Y. Zhang, C. Gong, F. Li, X. Meng, X. Hu, Z. Yuan, F. Wang and Y. Chen, *Advanced Materials*, 2022, 34, 2201840.
52 M. Park, S. C. Hong, Y.-W. Jang, J. Byeon, J. Jang, M. Han, U. Kim, K. Jeong, M. Choi and G. Lee, *Int. J. of Precis. Eng. and Manuf.-Green Tech.*, 2023, 10, 1223–1234.
53 L. A. Castriotta, R. Fuentes Pineda, V. Babu, P. Spinelli, B. Taheri, F. Matteocci, F. Brunetti, K. Wojciechowski and A. Di Carlo, *ACS Appl. Mater. Interfaces*, 2021, 13, 29576–29584.
54 Z. Li, T. R. Klein, D. H. Kim, M. Yang, J. J. Berry, M. F. A. M. van Hest and K. Zhu, *Nat Rev Mater*, 2018, 3, 18017.
55 A. Wąsiak-Maciejak, Ł. Przypis, W. Żuraw, K. Rycek, P. Janicka, M. Ścigaj, K. Dyk, H. Lai, A. Piejko, D. Pucicki, F. Fu, V. Kinzhybalo and K. Wojciechowski, *J. Mater. Chem. A*, 2025, 13, 7335–7346.
56 O. Y. Gong, G. S. Han, S. Lee, M. K. Seo, C. Sohn, G. W. Yoon, J. Jang, J. M. Lee, J. H. Choi, D.-K. Lee, S. B. Kang, M. Choi, N.-G. Park, D. H. Kim and H. S. Jung, *ACS Energy Lett.*, 2022, 7, 2893–2903.
57 B. Zhou, P. Zhao, J. Guo, S. Hu, X. Guo, J. Liu and C. Li, *Energy Environ. Sci.*, 2025, 18, 9865–9876.
58 M. Saliba, T. Matsui, J.-Y. Seo, K. Domanski, J.-P. Correa-Baena, M. K. Nazeeruddin, S. M. Zakeeruddin, W. Tress, A. Abate, A. Hagfeldt and M. Grätzel, *Energy Environ. Sci.*, 2016, 9, 1989–1997.
59 T. Bu, J. Li, H. Li, C. Tian, J. Su, G. Tong, L. K. Ono, C. Wang, Z. Lin, N. Chai, X.-L. Zhang, J. Chang, J. Lu, J. Zhong, W. Huang, Y. Qi, Y.-B. Cheng and F. Huang, *Science*, 2021, 372, 1327–1332.
60 F. Cheng, X. Jing, R. Chen, J. Cao, J. Yan, Y. Wu, X. Huang, B. Wu and N. Zheng, *Inorg. Chem. Front.*, 2019, 6, 2458–2463.
61 J.-W. Lee, Z. Dai, C. Lee, H. M. Lee, T.-H. Han, N. De Marco, O. Lin, C. S. Choi, B. Dunn, J. Koh, D. Di Carlo, J. H. Ko, H. D. Maynard and Y. Yang, *J. Am. Chem. Soc.*, 2018, 140, 6317–6324.
62 V. Romano, L. Najafi, A. A. Sutanto, G. Schileo, V. Queloz, S. Bellani, M. Prato, S. Marras, M. K. Nazeeruddin, G. D'Angelo, F. Bonaccorso and G. Grancini, *ChemPlusChem*, 2021, 86, 1044–1048.
63 L. Huang, Z. Hu, J. Xu, K. Zhang, J. Zhang and Y. Zhu, *Solar Energy Materials and Solar Cells*, 2015, 141, 377–382.
64 M. A. Truong, T. Funasaki, L. Ueberricke, W. Nojo, R. Murdey, T. Yamada, S. Hu, A. Akatsuka, N. Sekiguchi, S. Hira, L. Xie, T. Nakamura, N. Shioya, D. Kan, Y. Tsuji, S. Iikubo, H. Yoshida, Y. Shimakawa, T. Hasegawa, Y. Kanemitsu, T. Suzuki and A. Wakamiya, *J. Am. Chem. Soc.*, 2023, 145, 7528–7539.
65 B. Zhang, F. Guo, J. Xue, L. Yang, Y. Zhao, M. Ge, Q. Cai, B. Liu, Z. Xie, D. Chen, H. Lu, R. Zhang and Y. Zheng, *Sci Rep*, 2017, 7, 17695.
66 B. P. Dhamaniya, P. Chhillar, A. Kumar, K. Chandratre, S. Mahato, K. P. Ganesan and S. K. Pathak, *ACS Omega*, 2020, 5, 31180–31191.
67 W. Zhu, M. Yang, T. Han, Y. Wang, X. Luo, W. Chai, H. Xi, L. Zhou, D. Chen, J. Zhang, C. Zhang and Y. Hao, *Chemical Engineering Journal*, 2024, 500, 156798.
68 R. Wang, X. Liu, S. Yan, N. Meng, X. Zhao, Y. Chen, H. Li, S. M. H. Qaid, S. Yang, M. Yuan and T. He, *Nat Commun*, 2024, 15, 8899.
69 H. Chen, A. Maxwell, C. Li, S. Teale, B. Chen, T. Zhu, E. Ugur, G. Harrison, L. Grater, J. Wang, Z. Wang, L. Zeng, S. M. Park, L. Chen, P. Serles, R. A. Awni, B. Subedi, X. Zheng, C. Xiao, N. J. Podraza, T. Filleter, C. Liu, Y. Yang, J. M. Luther, S. De Wolf, M. G. Kanatzidis, Y. Yan and E. H. Sargent, *Nature*, 2023, 613, 676–681.
70 S. Li, Z. Liu, Z. Qiao, X. Wang, L. Cheng, Y. Zhai, Q. Xu, Z. Li, K. Meng and G. Chen, *Advanced Functional Materials*, 2020, 30, 2005846.
71 C. Liu, Y. Yang, H. Chen, J. Xu, A. Liu, A. S. R. Bati, H. Zhu, L. Grater, S. S. Hadke, C. Huang, V. K. Sangwan, T. Cai, D. Shin, L. X. Chen, M. C. Hersam, C. A. Mirkin, B. Chen, M. G. Kanatzidis and E. H. Sargent, *Science*, DOI:10.1126/science.adk1633.
72 J. Wang, Y. Wu, J. Zhao, S. Lu, J. Lu, J. Sun, S. Wu, X. Zheng, X. Zheng, X. Tang, M. Ma, S. Yue, K. Liu, Z. Wang and S. Qu, *Small Methods*, 2024, 8, 2400043.
73 X. Zheng, T. Jiang, L. Bai, X. Chen, Z. Chen, X. Xu, D. Song, X. Xu, B. Li and Y. (Michael) Yang, *RSC Adv.*, 2020, 10, 18400–18406.
74 Z. Zheng, Z. Xue, K. Zhao, Y. Yang, X. Zhu, H. Li, S. Cheng, S. Li, N. Yan and Z. Wang, *Solar RRL*, 2024, 8, 2301076.
75 R. Witteck, D. Nguyen Minh, G. Paul, S. P. Harvey, X. Zheng, Q. Jiang, M. Chen, T. Abzieher, A. F. Palmstrom, B. Habersberger, E. A. Gaulding, J. M. Luther and L. M. Wheeler, *ACS Appl. Energy Mater.*, 2024, 7, 10750–10757.
76 P. Basumatary, J. Kumari and P. Agarwal, *AIP Conf. Proc.*, 2021, 2369, 020022.
77 A. Mavlonov, Y. Hishikawa, Y. Kawano, T. Negami, A. Hayakawa and T. Minemoto, *Solar Energy Materials and Solar Cells*, 2025, 282, 113410.
78 N. Krobkrong, A. Mavlonov, Y. Hishikawa, Y. Kawano, T. Negami and T. Minemoto, *Materials Science in Semiconductor Processing*, 2026, 203, 110247.
79 A. Mavlonov, Y. Hishikawa, Y. Kawano, T. Negami, A. Hayakawa, S. Tsujimura, T. Okumura and T. Minemoto, *Solar Energy*, 2025, 286, 113174.
80 S. Hu, J. Thiesbrummel, J. Pascual, M. Stolterfoht, A. Wakamiya and H. J. Snaith, *Chem. Rev.*, 2024, 124, 4079–4123.

81 Y. Wang, R. Lin, X. Wang, C. Liu, Y. Ahmed, Z. Huang, Z. Zhang, H. Li, M. Zhang, Y. Gao, H. Luo, P. Wu, H. Gao, X. Zheng, M. Li, Z. Liu, W. Kong, L. Li, K. Liu, M. I. Saidaminov, L. Zhang and H. Tan, *Nat Commun*, 2023, 14, 1819.
View Article Online DOI: 10.1039/D6EL00050A
82 P. Spinelli, R. Fuentes Pineda, M. Scigaj, T. Ahmad and K. Wojciechowski, *Appl. Phys. Lett.*, 2021, 118, 241110.

The supporting data has been provided as part of the Supplementary Information.

View Article Online
DOI: 10.1039/D6EL00050A